Korean J. Chem. Eng., 40(6), 1518-1528 (2023)
DOI: 10.1007/s11814-023-1423-1

pISSN: 0256-1115
eISSN: 1975-7220

Partial sulfur doping induced variation in morphology of $MnFe_2O_4$ with enhanced electrochemical performance for energy storage devices

Muhammad Abdullah*, Fatemah Farraj Alharbi, Rabia Yasmin Khosa***, Huda A Alburaih**, Sumaira Manzoor*, Abdul Ghafoor Abid****, Haitham Elhosiny Ali*****,******, Muhammad Suleman Waheed*******, Muhammad Numair Ansari****, and Hafiz Muhammad Tahir Farid********,†**

*Department of Chemistry, Government College University, Lahore
**Department of Physics, College of Science, Princess Nourah bint Abdulrahman University, P.O. Box 84428, Riyadh 11671, Saudi Arabia
***University of Education, Lahore, Dera Ghazi Khan Campus, D. G. Khan 32200, Pakistan
****Institute of Chemical Sciences, Bahauddin Zakariya University, Multan
*****Research Center for Advanced Materials Science (RCAMS), King Khalid University, Abha 61413, P.O. Box 9004, Saudi Arabia
******Physics Department, Faculty of Science, Zagazig University, Zagazig, Egypt
*******Centre of Excellence in Solid State Physics, University of the Punjab, Lahore 54590, Pakistan
********Department of Physics, Government College Taunsa Sharif- 32200, Pakistan
(*Received 6 November 2022 • Revised 26 January 2023 • Accepted 31 January 2023*)

Abstract−Manganese ferrite offers several advantages when employed as an electrocatalytic material for supercapacitors, including outstanding cycle stability and energy capacity. When compared to identical-metal sulfides, specific capacitance (C_{sp}) of $MnFe_2O_4$ remains inadequate. So, using the hydrothermal synthesis technique, partial sulfur doping of $MnFe_2O_4$ was achieved to investigate the synergetic effect of oxides and sulfides. Various spectroscopic and microscopic studies demonstrate that adding sulfur atoms into $MnFe_2O_4$ increases the lattice parameters, which improves electrochemical performance. At a current density around 2 A g^{-1}, then calculating $MnFe_2O_4$ with partial sulfur doping has a C_{sp} of 1,201.60 F g^{-1}, that is greater than 784.0 F g^{-1} of pure $MnFe_2O_4$. Maximum energy density (E_d) of 93.62 Wh kg^{-1} was produced with a power density (P_d) of 749 W kg^{-1}. The current study depicts that partial sulfur doping can enhance the electrochemical behavior of $MnFe_2O_4$. As a result, the present work shows more effective in field of energy storage by enhancing their poor electrochemical performance.

Keywords: $MnFe_2O_4$, Electrochemical Performance, Hydrothermal Synthesis, Sulfur Doping

INTRODUCTION

Supercapacitors have a vital role in fields related to energy storage owing to quick (charge-discharge) rate, exceptional cycle stability along with higher power density (P_d). Supercapacitors offer a greater range of potential applications in sectors of electric vehicles, portable electronics along with grids [1-8]. They can boost energy consumption efficiency when coupled along with batteries that requires high energy density (E_d). Firm basis on their energy storage mechanism, supercapacitors additionally diversified as electrochemical double-layer capacitors (EDLC) along with pseudocapacitors [9-15]. EDLC use electrostatic (adsorption/desorption) mechanism to store energy, whereas pseudocapacitors are expected to primarily use faster along with a invertible electrochemical faradaic reaction. These two categories of supercapacitors device to be constrained in their development by their low energy densities [16-19].

Research on electrode materials has attracted much interest since it is an essential aspect that is strongly tied to its energy density. More and more materials are being developed with outstanding qualities and a large number of possible applications. Transition metal oxides (TMOx) and transition metal sulfides (TMS) have drawn greater attraction because of higher theoretical energy density, low toxicity, along with abundancy of deposits [20-24]. Transition metal oxides like iron oxide, manganese oxide and nickel oxide, are recognized as excellent options for supercapacitor electrode materials, building on the success of RuO_2. This binder-free and freestanding nickel oxide@Ni Foam anchored porous carbon supercapacitor electrode was created by Deng et al. via a combination of pyrolysis, temperature-controlled phase separation along with hydrothermal reaction. It was determined that the sample had C_{sp} of 152 F g^{-1} despite being loaded with a relatively large amount of active substances (14.98 mg cm^{-2}) [25]. Larger C_{sp} around 264 F g^{-1} @ 1 A g^{-1} was exhibited by Ferric oxide@C nanoparticles made by Zheng et al. used straightforward along with co-precipitation and carbonization technique. Rate capability around 90.1% more than (CV

†To whom correspondence should be addressed.
E-mail: tahirfaridbzu@gmail.com

cycle of 5,000) further demonstrated the device's high cyclic stability [26]. Xinhua et al. studied (electrochemical properties) related to MnO_2 nanoparticles by electrospinning deposition for C_{sp} application. Fabricated electrode showed C_{sp} around 645 F g^{-1} at 0.5 A g^{-1} and showed better stability having more than 20 K cycles [27]. Hydrothermally produced NiO nanoflakes were examined and reported on by Mali et al. who looked into the impact of urea concentration on NiO's shape. The results showed that NiO's specific capacitance was highest at ratio of 1 : 2 (Ni : urea) and sweeping speed around 10 mV s^{-1} [28]. Zhou et al. synthesized (manganese oxide derived) porous carbon nanofiber electrode via an electrospinning approach for energy storage application. Electrochemical efficiency of MnO_2/CN electrode displaying a C_{sp} of 520 F g^{-1} around 0.5 A g^{-1} showed 92.3% rate of capability afterwards 4,000 cycles under 6.0 M potassium hydroxide [29]. Kai-Hang et al. developed MnO_2/reduced graphene oxide (RGO) nanocomposites via electrochemical deposition approach for energy storage application. Their electrochemical analysis represents areal specific capacitance around 14 F cm^{-2} at 2 mV s^{-1} [30]. Chen et al. developed C_{sp} of 425 F g^{-1} and displayed better stability above 3,000 cycles for capacitive performance [31]. Raj et al. studied electrochemical behavior related to flower type MnO_2 and their result revealed that the electrocatalytic material contains the Cs around 160 F g^{-1} @ 1 A g^{-1} [32].

Fast migration of ions along with electrons present in TMOx is challenging because of their naturally poor electrical conductivity, which results in unfavorable electrochemical performance. Bimetallic oxides have more conductivity and capacity than single metal oxides. Bimetallic oxides of the type $MnFe_2O_4$ (MFO) have an inverted spinel structure. Half amount of Fe^{3+} ions occupied tetrahedral gaps and remaining half together with all Mn^{2+} ions, inhabited octahedral voids. Several scientists discovered the metal Fe_2O_4 such as $NiFe_2O_4$ was fabricated by hydrothermal approach via Gao et al. for energy storage conversion. The greater C_{sp} of 240.9 F g^{-1} and exhibited 128% over 2,000 cycles. Furthermore, the practical applicability of $NiFe_2O_4$ was investigated with two electrode system. The Ni based spinel exhibited the energy density of 10.15 Wh Kg^{-1} and P_d of 140 W Kg^{-1} [33]. The $ZnFe_2O_4$ synthesized by Shrikant et al. with SILAR strategies. The results revealed that the $ZnFe_2O_4$ ex- hibited the C_{sp} of 471 F g^{-1} under 1 NaOH @ 5 mV s^{-1} and exhibited good P_d and E_d [34]. The $CuFe_2O_4$ was developed by Guo et al. for energy storage application. The $CuFe_2O_4$ nanoparticles exhibited the C_{sp} of 473 F g^{-1} @ 40 mV s^{-1} under 0.5 M sulphuric acid with rate capability of 88.6% over 2,000 cycles. Maitra et al. synthesized the $NiFe_2O_4$ via sol gel nanoparticles for capacitive performance. The materials exhibited the Cs of 61 F g^{-1} and E_d of 41 Wh Kg^{-1} and cyclic retention of 82.91% over 1,000 cycles [35]. Fei et al. discovered the electrochemical properties of $MnFe_2O_4$ for energy storage application. The fabricated materials exhibited the high capacity of 302.6 mC cm^{-2} and E_d of 68.7 mWh cm^{-2} having a good cyclic stability of 50 s [36]. Among ferrites, including MFe_2O_4 where M=Cu, Ni, Co, or Zn, manganese ferrite ($MnFe_2O_4$) has been reported to display higher capacitance value than other ferrites [37-39]. The superior properties of $MnFe_2O_4$ are attributed to the varied redox state, low cost, abundant availability, high cycling stability, fascinating magnetic property, high power delivering capability and greater capacitance value, which make it a suitable candidate for supercapacitor application [40-43]. Despite the many potential benefits, $MnFe_2O_4$ exhibited the weak electrical conductivity that restrict the employment in supercapacitor application. However, the electrochemical efficiency of manganese spinel ferrite was increased by adopting the doping strategy of several chalcogenides [44-47].

Scholars discovered about transition metal sulfides: they acquire greater electrical conductivity and more redox sites as compared to oxides as their studies progress. Yujin et al. synthesized dual N, S-doped $CoFe_2O_4$@carbon nanotube via hydrothermal procedure for C_{sp} application. Electrode material related to $N_2S_{1-x}CoFe_2O_4$@CNTs depicts electrochemical efficiency of 1053.60 F g^{-1} at 1 A g^{-1} under 1 M potassium hydroxide electrolyte. Moreover, the rate retention attained 93.15% @ 30 A g^{-1} afterwards 5,000 cycles [48]. Partial sulfur doped $NiFe_2O_4$ was fabricated via hydrothermal approach by Xicheng et al. for energy storage application. C_{sp} of partial (sulfur doping $NiFe_2O_4$) was determined and it was around of 284 F g^{-1}, E_d of 21.14 Wh kg^{-1} P_d of 375 W kg^{-1} [49]. Jonghyun et al. fabricated S-doped NiFe-oxide nanostructure using hydrothermal-sulfurization technique. After sulfurization, NiFeS-NFs demonstrated an enhancement in their C_{sp} of NFs, afterwards sulfurization increased in range of 69 to 604 F g^{-1} at 1 A g^{-1} [50]. C doped $ZnFe_2O_4$ was prepared via hydrothermal route for supercapacitor application are reported by Lei Li et al. Fabricated electrode displayed C_{sp} 244 F g^{-1} at very small current density with rate capability around 83.9% [51]. S-doped zinc-nickel-cobalt oxides (S-ZNCO) was prepared by Yajie et al. via hydrothermal treatment along with sulfurization method. It was observed that doping increased active sites in redox reaction and enhanced C_{sp} of 2,919.60 F g^{-1} around 1 A g^{-1}. Assembled S-ZNCO-NF//AC device attained higher E_d around 72.970 W h kg^{-1} at power density of 825.0 W kg^{-1} [52]. Dakshana et al. made $NiCo_2S_4$ nanoparticles (NPs) by hydrothermal method using thiourea and thioacetamid, separately. Electrochemical behavior of $NiCo_2S_4$/Ni foam electrode showed higher C_{sp} values around 1,051.49 C g^{-1} compared with NTU-$NiCo_2S_4$ (690 C g^{-1}) @ 2 A g^{-1}. In addition, NTA-$MnCo_2S_4$ held retention around 98% after 10,000 GCD cycles @ 6 A g^{-1} [53]. Sulfides commonly break down gradually with ongoing charging and discharging in an (alkaline) electrolyte, which has a negative impact on cycle retention.

Herein, partial sulfur doped MFO was synthesized using hydrothermal synthesis, bringing together benefits of oxides along with sulfides. Increasing d-spacing related to lattice plane after partial sulfur doping has been shown to increase electrochemical performance without significantly altering the structure of the lattice. Electrochemical performance of samples was evaluated in three and two electrode configurations under potassium hydroxide solution. The electrochemical results revealed the C_{sp} of (1,201.60 F g^{-1}) at 2 A g^{-1} and rate performance (95.82% at 2 A g^{-1}) of partial sulfur doped MFO out- performed the electrochemical behavior of MFO. Additionally, the two-electrode system that used active carbon (AC) worked as cathode electrode species, and partial sulfur doped MFO as (positive electrode) material had a fantastic retention capacitance rate (94.82%) after 5,000th GCD cycles. Comparatively, partial sulfur doping technique may improve C_{sp} and (conductivity of oxides), meanwhile decreasing (Sulphur-related) cycle performance deterioration.

EXPERIMENTAL SEGMENT

1. Fabrication of $MnFe_2O_4$ (MFO)

First, 50 mL of (DI water) was used to dissolve 0.1 M (0.894 g) of manganese nitrate ($Mn(NO_3)_2{\cdot}4H_2O$, Sigma Aldrich, 98%), 0.2 M (2.41 g) of ferric nitrate ($Fe(NO_3)_3{\cdot}9H_2O$, Sigma Aldrich, 99.99%). 0.1 M (0.9 g) of D (+) glucose ($C_6H_{12}O_6$, Merck, 97.5%) and 0.1 M (0.3 g) of urea (CHN_2O, Merck 99.0%) The mixture was then stirred magnetically for nearly 1.5 h. Well combined aqueous solution was then put into an autoclave lined with polytetrafluoroethylene and put in electric furnace at 393.15 K in vacuum oven for 10 h. Precursor was then recovered by centrifugation at 10,000 rpm and rinsed with DI water by suction filtering after naturally cooling at room temperature. Dried product was then further annealed for 3 h at 573.15 K and saved for further synthesis and characterization purposes.

2. Synthesis of Partial S Doping $MnFe_2O_4$

In the typical synthesis, partial sulfur doped MFO (MFO-S) was produced via hydrothermal process. At first, the as synthesized MFO was poured into beaker containing 0.1 M (0.39 g) of Na_2S solution in 50 mL of DI H_2O, accordingly. This solution was then mechanically stirred and ultrasonically dispersed for 1 h before being transferred towards the autoclave. At 393.15 K for 4 h, simple hydrothermal reaction occurred. The MFO-S sample was then cleaned using suction filtration and acquired after drying for 8 h at 333.15 K.

3. Physiochemical Characterizations

Structural features, chemical content and elemental valance state of the produced materials were assessed using X-ray diffraction (XRD, Advance D8 Bruker), Fourier transform infrared spectroscopy (FTIR, JASCO 6800) and X-ray photoelectron (XPS, PHI 5300). Morphological characterization was then estimated utilized as scanning electron microscope and energy-dispersive spectroscopy (SEM-EDX, Quanta 200 FEG). The specific surface area (SSA) along with pore size dispersal was then obtained via Brunauer-Emmett-Teller and Barrett, Joyner, and Halenda method (BET-BJH, Quantachrome 2200e).

4. Fabrication of Electrocatalytic Species for Electrochemical Measurements

First, nickel foam was washed using an ultrasonic process at 5 min with 2 M HCl, acetone, along with ethanol. The Ni foams were then proceeded to dry in vacuum for 6 h at 60 °C. Three-electrode system's electrode materials were created by combining carbon black, polyvinylidene difluoride (PVDF), and MFO or MFO-S in a 9 : 1 : 1 ratio. The combination was equally deposited on the Ni foam that served as the current collector after being evenly dissolved in 1-Methyl-2-pyrrolidinone (NMP). Finally, electrode was dried in vacuum for 10 h at 60 °C. Preparation of positive electrode for the two-electrode system was exactly the same as described above, but production of negative electrode required replacing MFO or MFO-S along with active carbon (AC). The total weight of electrode materials was roughly 2.5 mg for all electrodes.

5. Electrochemical Measurements

Both three-electrode system along with two-electrode system electrochemical tests were performed on MFO and MFO-S samples. A PG-STAT 204 electrochemical station (Netherlands) was used for measuring electrochemical efficiency of hybrid material and its counterparts under 1.0 M KOH, which served as electrolyte. Conventional saturated silver/AgCl electrode was used as standard electrode in a three-electrode setup, and 1×1 cm^2 Pt electrode was employed as axillary electrode. The frequency ranges for impedance measurement were then set to be between 100 Hz and 100 KHz. In two-electrode system, the MFO-S or MFO electrode was utilized as anode electrode. However, AC electrode employed as cathode electrode. Following equation was then used to get specific capacitance of the fabricated material [54].

$$C_{sp} = \frac{\int_{vc}^{va} I \times dV}{m \times S \times \Delta V} \tag{1}$$

In which, C_{sp} represents specific capacitance (F g^{-1}), $\int_{vc}^{va} I \times dV$ represents the area, m is mass of electrode materials (g), S is sweeping speed and V is voltage (V). The experiments using galvanostatic charge-discharge polarization were also employed for measuring specific capacitance (C_{sp}), energy density (E_d), and power density (P_d) with help of given equation [55].

$$C_{sp} = \frac{I \times \Delta t}{m \times \Delta V} \tag{2}$$

$$E_d = \frac{Cp \times \Delta V^2}{7.2} \tag{3}$$

$$P_d = \frac{E \times 3{,}600}{\Delta t} \tag{4}$$

Further GCD data was employed for measuring specific capacity of all fabricated substances with following relation.

$$\text{Sp. capacity} = \frac{I \times t}{m} \tag{5}$$

Herein, Eq. (2), (3), (4) and (5) represent the t=time, I=current (A), V=potential, m=mass of the conductive substrate, E_d=energy density, C_{sp}=specific capacitance, P_d=power density.

Electrochemical active surface area was then used to measure Cdl by dividing the anodic and cathodic potential. The obtained Cdl value was converted into ECSA with below Eq. (6) [21,56-61].

$$ECSA = \frac{C_{dl}}{C_{sp}} \tag{6}$$

EIS technique was then employed to measure resistivity of fabricated material ranging from 100 Hz to 100 KHz @ 0.55 V (Ag/AgCl). Stability of hybrid substance was then determined around 0.75 V (Ag/AgCl) for 50 h under 2 M KOH with chronoamperometry.

RESULTS AND DISCUSSION

Phase crystallinity of samples before and after partial sulfur doping was evaluated via XRD analysis, as illustrated in Fig. 1(a). Crystal phase of MFO present in the diffraction angle at 18.16°, 30.24°, 35.43°, 43.34°, 54.15°, 57.27°, 63.51° and 74.74° are corresponding to hkl value of (111), (222), (311), (400), (422), (511), (440) and (533) displaying the cubic crystal system and their results are well consistent with the PDF no.: 01-073-1964. The MFO display the

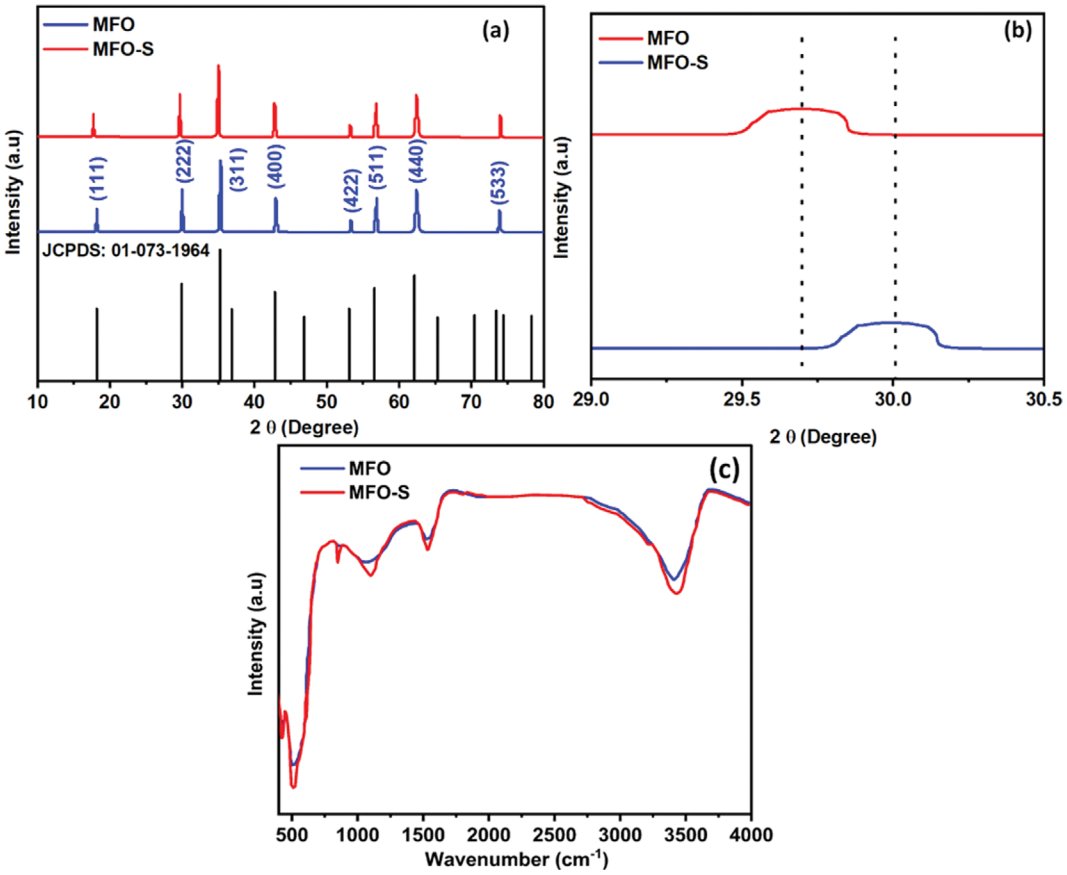

Fig. 1. (a) XRD diffraction peaks, (b) Magnified XRD diffractogram and (c) FTIR spectra of MFO and MFO-S.

space number of 227, space group of Fd-3m, and crystal lattice parameter of a=b=c=8.51 A°. Furthermore, the sample's phase did not change after partial sulfur doping, indicating that the sample's makeup was still MFO. By comparing XRD data of fabricated materials before and after doping of partial sulfur in range of 30.05° to 29.69° shows a small variation in the angle of diffraction indicates the successful incorporation of sulfur and magnified XRD diffractogram represented in Fig. 1(b). The average crystallite size (D) of the MFO and MFO-S of 64 nm and 42 nm was computed with Debye Scherrer equation as given below [20,62,63].

$$D = \frac{K\lambda}{\beta\cos\theta} \tag{7}$$

Herein, D represents crystallite size (nm), K represents the Scherrer constant (0.9 shape factor) λ represent wavelength of X-ray (Cu Kα=1.5046 A°), β is maximum breadth at half maxima of diffraction pattern (FWHM), and θ represents angle of diffraction.

The FTIR spectrum of MFO fabricated materials after and before partial "s" doping ranging from 400 to 4,000 cm^{-1} are mentioned in Fig. 1(b). Strong absorption bands are seen in the spectra of MFO and MFO-S at 420.8 and 527.2 cm^{-1}, that show association with vibration modes of the metal atoms in tetrahedral and octahedral sites, respectively (M_{td}↔O and M_{oh}↔O). Additionally, bending vibration of H_2O and stretching modes of hy- droxyl group in absorbed or free H_2O induce absorption bands at 1,527.1 and 3,437.1 cm^{-1} [64]. It is measured that an absorption curve exists at 1,122.6 cm^{-1} in MFO-S attributed to bending vibration of the sulfides group, despite the fact that it does not clearly appear in MFO.

Chemical make-up along with element valence of MFO electrode materials before and after partial sulfur doping was investigated using XPS analysis (d-f). Wide-scan XPS spectra of MFO and MFO-S clearly reveal the distinctive Fe, Mn, and O element peaks, as illustrated in Fig. 2(a). However, a distinct S element peak may be detected in MFO-S but not in MFO. This demonstrates that MFO sample was favorably doped with the S element following partial sulfur doping. Gaussian fitting was used for acquiring deconvolutions of all these peaks in the context to precisely examine dispersal and valence state of the iron, manganese, sulfur and oxygen elements in samples. The fitted Fe 2p spectra for the two samples are shown in Fig. 2(b). We are well aware that in spinel ferrite, transition metal ions fill the tetrahedral and octahedral voids. In general, octahedral coordination elements have lesser binding energy than tetrahedral coordination elements. XPS band of Fe $2p_{3/2}$ and Fe $2p_{1/2}$ may be fragmented into two curves belonging to Fe^{2+} in B site, as well as Fe^{3+} in A site, as represented in Fig. 2(b). Fe $2p_{3/2}$ spectra specifically contain peaks around energies of 711.3 (Fe^{2+} in B site) and 714.9 (Fe^{3+} in A site). Additionally, peaks seen around 720.8, 722.4, 729.5 and 733.1 eV can independently interact with Fe^{2+} at the B site, and Fe^{3+} in the A site to form curve of Fe $2p_{1/2}$. To conclude, two samples contain iron in valence states of Fe^{2+} and Fe^{3+}. The conduction mechanism of MFO may be ex-

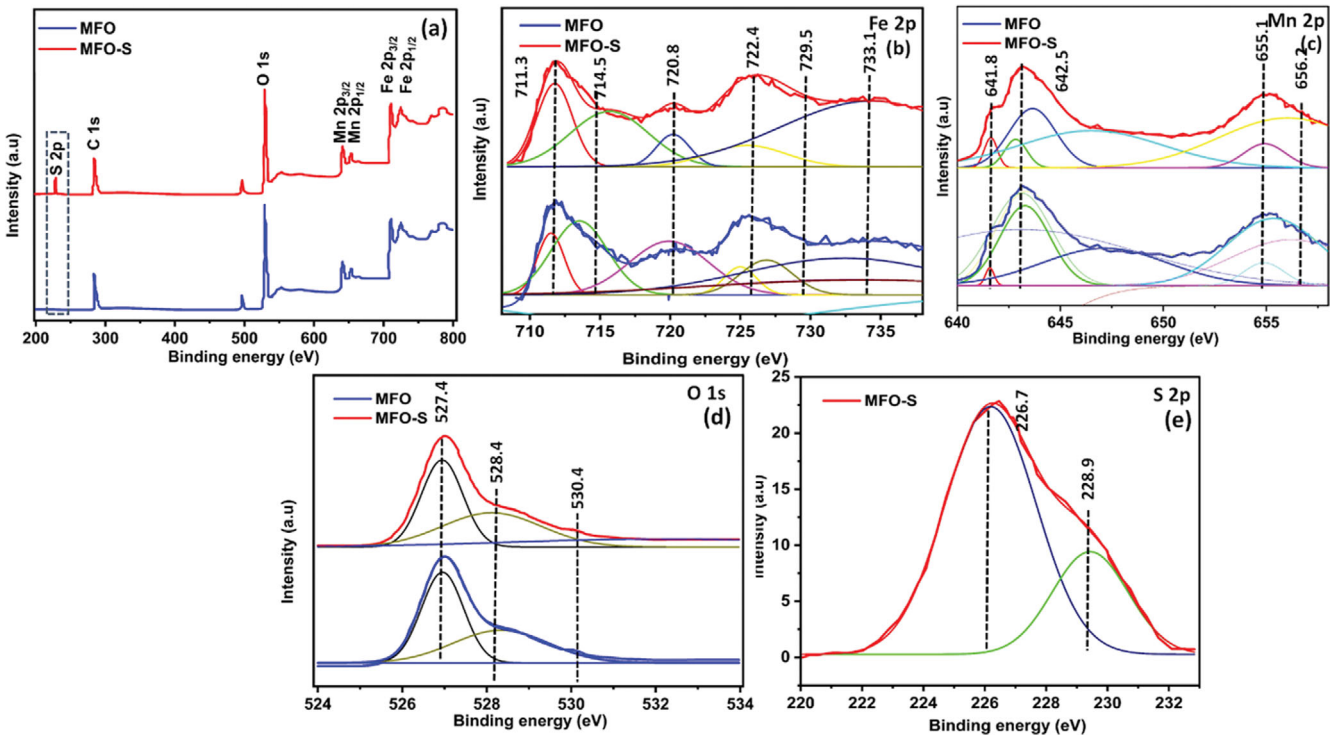

Fig. 2. (a) Wide XPS spectra, (b) deconvoluted Fe 2p, (c) Mn 2p, (d) O 1s and (e) S 2p.

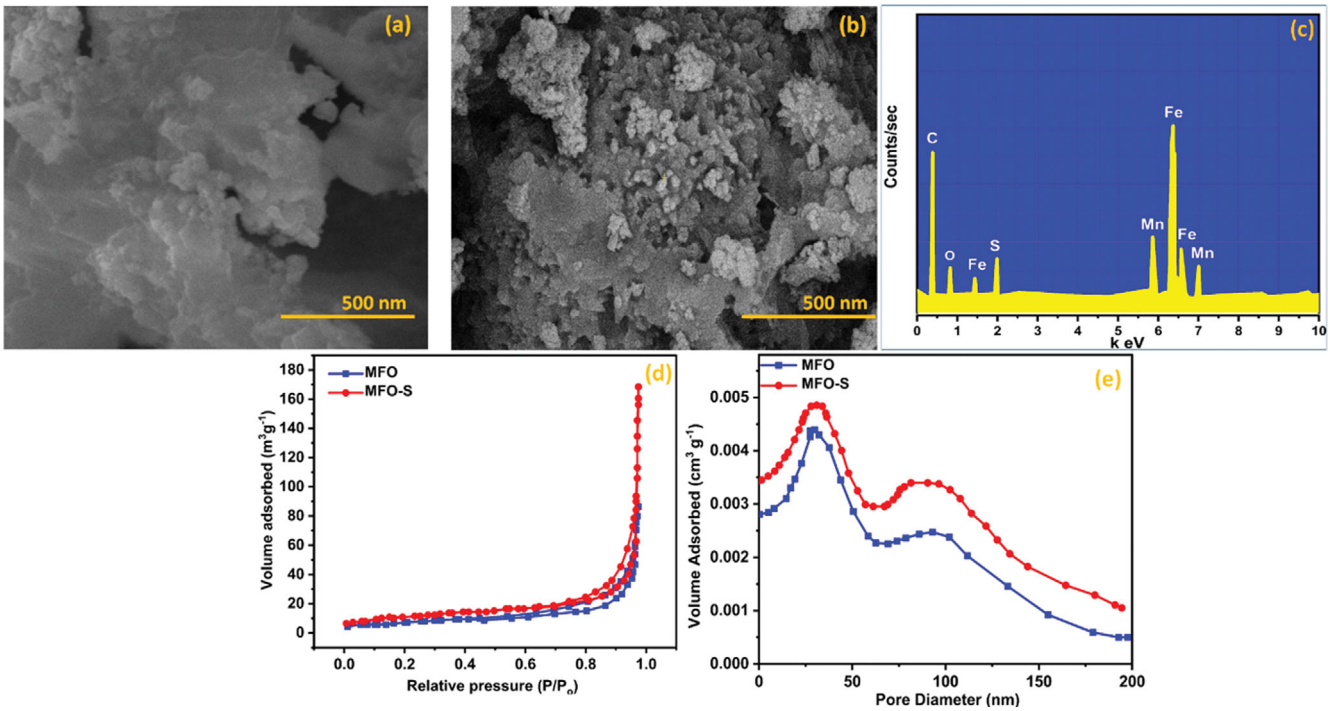

Fig. 3. SEM image of (a) MFO, (b) MFO-S, (c) EDX spectrum of MFO-S, (d) BET isotherm and (e) Pore size distribution of MFO and MFO-S, respectively.

plained by the theory of electron hopping, that could be understood as electrons hopping among various valences of same elements. As a result, the presence of Fe^{2+}/Fe^{3+} might improve conduction of two samples, which is thought for improving electrochemical performance in supercapacitor application. Peak of Mn $2p_{3/2}$ might get separated into (two deconvolutions) around 641.8 and 642.5 eV, which corresponded towards Mn^{2+} in octahedral voids (B site) along with tetrahedral voids (A site), respectively, as

seen in Fig. 2(c). Also included in peak of Mn $2p_{1/2}$ are peaks around 655.1 eV (Mn^+ in the B site) and 656.2 eV (Mn^{2+} in the A site). The XPS of oxygen 1s as well as its fragmented are mentioned in Fig. 2(d). It is believed that the peak at 527.4 eV represents a normal M-O bond. Additionally, some surface flaws like hydroxyl groups or oxygen adsorbed on the surface are accountable for the curve at 528.5 eV. In addition, H_2O's physical or chemical absorption is responsible for the peak at 530.4 eV. The two samples were subjected to XPS measurements between 226.7 eV and 228.9 eV for demonstrating successful instigation of element S via partial sulfur doping. S 2p curve along its deconvolutions of MFO-S is depicted in Fig. 2(e). The results indicate that MFO does not exhibit a peak in this range; however, MFO-S has an apparent peak of sulfur element.

We are all aware morphologies of electrode substances, which have direct impact on contact area among electrocatalytic species and electrolyte, are intimately related to their electrochemical characteristics. SEM pictures of the acquired MFO samples before and after partial sulfur doping are mentioned in Fig. 3(a)-(b). Fig. 3(a) demonstrates that hydrothermal fabricated MFO exhibited the agglomerated nanoparticles and partial sulfur doping tuned the morphology of MFO-S as represented in Fig. 3(b). The tuned morphology provides greater interfacial area with random distribution of nanoparticles, and resultant increase of the electrochemical efficiency of doped material. Existence of all elements like manganese, oxygen, iron, carbon and sulfur elements in the MFO-S shows the successful formation of the composite measured by energy dispersive X-ray (EDX) as mentioned in Fig. 3(c).

As is widely known, redox reaction occurring at the surface of electrode substances serves as mechanism of energy storage for pseudocapacitors. Contact area among electrode substances and electrolyte will therefore be impacted by specific surface area, which will have impact on electrochemical performance. N_2 adsorption and desorption spectra of MFO as well as MFO-S are mentioned in Fig. 3(d). In comparison to sample MFO, whose specific surface area was determined around 43.2 $m^2\ g^{-1}$, sample MFO-S depicts a greater specific surface area around 68.42 $m^2\ g^{-1}$, that may be caused by a little surface fracture during the partial sulfur doping procedure. The average pore diameters of MFO as well as MFO-S, which are (mesoporous substances) for two samples, are measured by the Barrett, Joyner, and Halenda (BJH) method 25.23 nm and 82.32 nm, respectively, according to the results. Pore size distribution curves of MFO and MFO-S are also mentioned in Fig. 3(e).

1. Electrochemical Analysis

By using three-electrode configure with Pt electrode as axillary, an Ag/AgCl as standard electrode (along with salt bridge of 3.0 M KCl as electrolyte) and 1.0 M potassium hydroxide as electrolyte, electrochemical characteristics of the produced MFO and MFO-S were examined from −0.1 to 0.8 V (silver/silver chloride), as mentioned in Fig. 4(a)-(b). CV analysis shows that, CV polarization

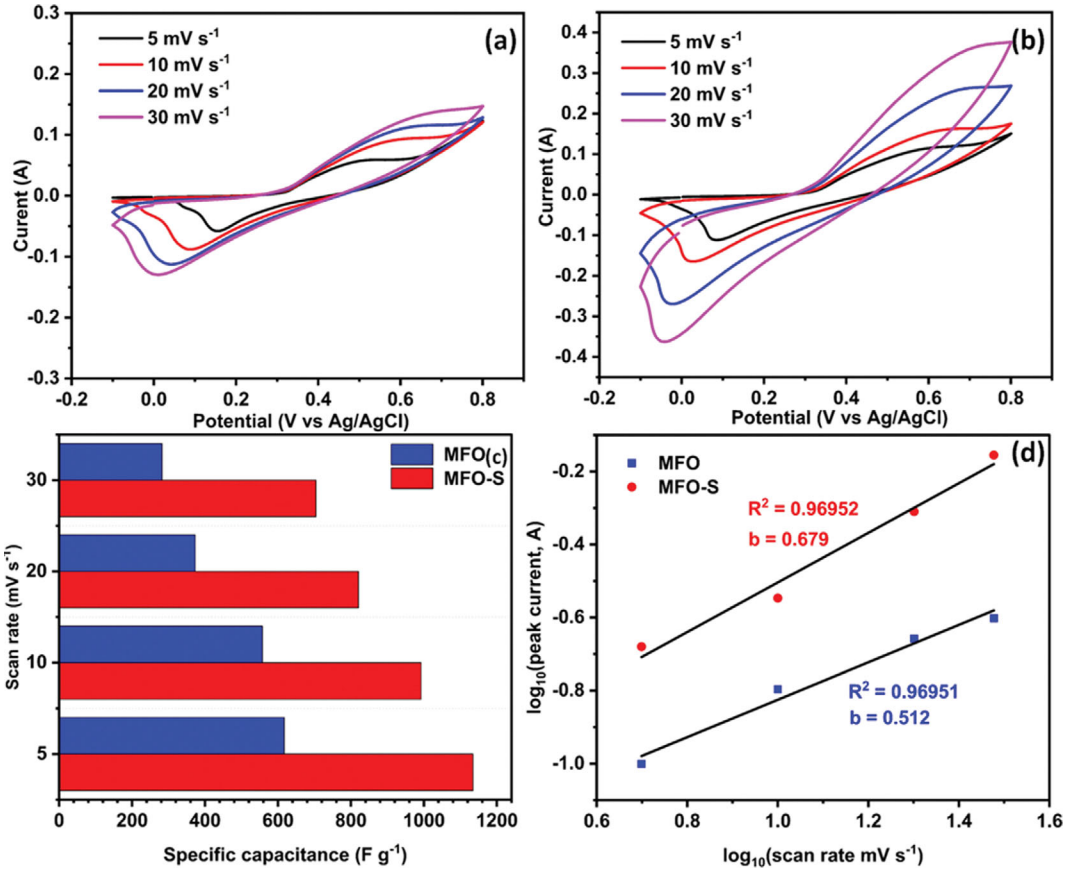

Fig. 4. Voltammagram of (a) MFO, (b) MFO-S, (c) Plot of C_{sp} vs sweeping speed and (d) plot function of $\log_{10}$ (sweeping speed) vs $\log_{10}$ (peak current).

curves of both samples exhibit distinct redox peaks that correspond to the conventional battery-like properties. According to the following, Eq. (8), the redox processes of Mn^{2+}/Mn^{3+} and Fe^{2+}/Fe^{3+} contribute to the redox peaks:

$$MnFe_2O_4+H_2O+OH^- \rightarrow MnOOH+2FeOOH+e^- \quad (8)$$

When comparing the CV curves of both samples, the integral area of the MFO-S exhibited the largest surface area than the MFO, thus they show high specific capacitance. The C_{sp} of the MFO and MFO-S are 617.10 and 1,201.62 F g^{-1} estimated with Eq. (1) and graphical representation with regard to scan rates is illustrated in Fig. 4(c) and comparison among the reported material is display in Table 1. Larger C_{sp} of MFO-S was attributed towards larger surface area, enriched active site, diverse morphology and electron donating effect of sulfur. Additionally, it is believed that determination of CV contributed towards a reliable method for determining kinetics of electrochemical reactions. Following equation describes the correlation among scan rate and peak current [65].

$$i_p=av^b \quad (9)$$

Herein, i_p stands for the maximum current (A) and v for sweeping rate (mV s^{-1}). usually, b=1 denotes behavior control by capacitance process, while b=0.5 denotes behavior control via diffusion process. Fig. 4(d) displays plot of $\log_{10}(i)$ vs $\log_{10}(v)$, where the slopes of fitted lines denote values of b. The fact that both samples' b values are ±0.5 demonstrates that capacitive behavior mostly regulates

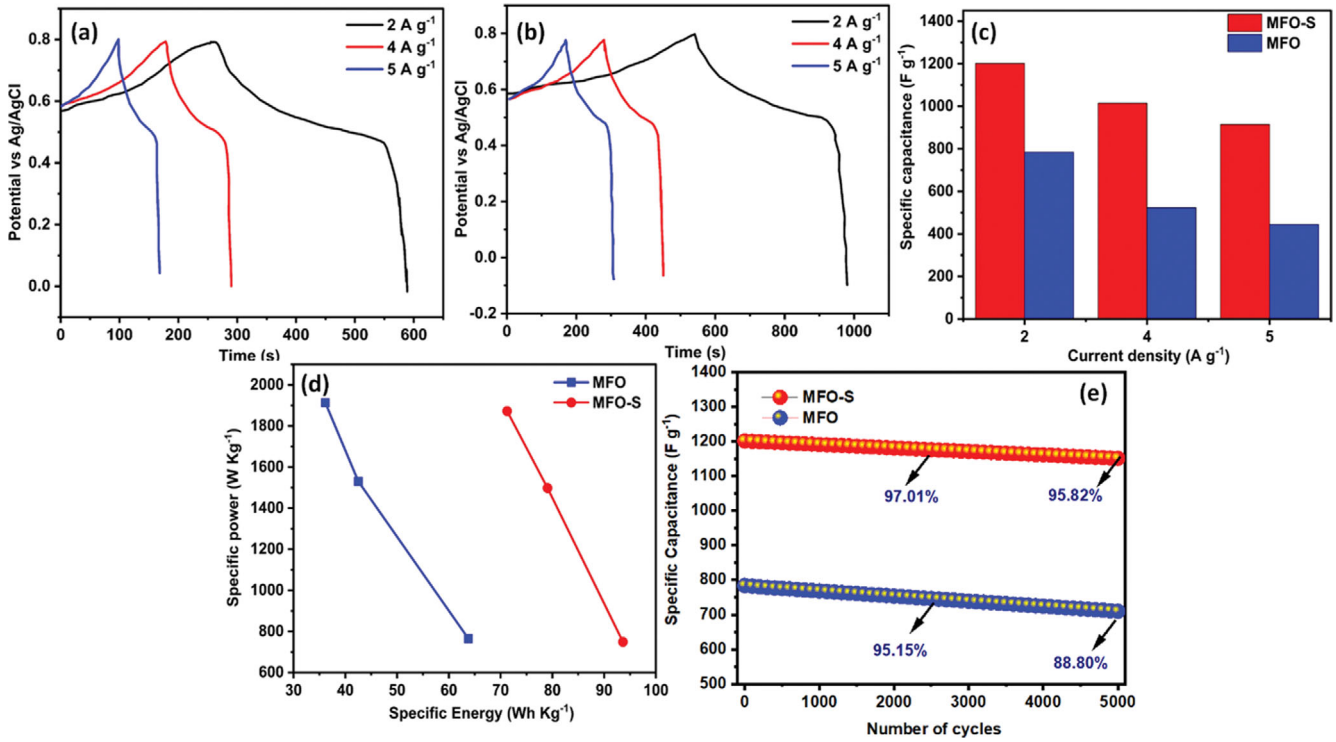

Fig. 5. GCD polarization curve of (a) MFO, (b) MFO-S, (c) C_{sp} plot profile of MFO and MFO-S, (d) Roenge plot of MFO and MFO-S, and (e) GCD stability curve of MFO and MFO-S electrodes.

Table 1. Comparison among the fabricated materials and reported literature

Sr. No.	Materials	Specific capacitance (C_{sp}) (F g^{-1})	Current density (A g^{-1})	Electrolytes	Ref.
1	N-doped $NiCo_2O_4$	2,986.25	2	KOH	[66]
2	partial S-doped $NiFe_2O_4$	284	1	KOH	[67]
3	$NiCo_2O_4$@NC	2,000.6	1	NaOH	[68]
4	$SrFe_2O_4$-NC	895	1	KOH	[69]
5	P-doped $MnCo_2O_4$	996.7	1	KOH	[70]
6	N-GE/$NiFe_2O_4$/PANI (NGNP)	667	5	KOH	[71]
7	P-doped $NiCo_2O_4$/$NiMoO_4$	2,334.0	1	KOH	[72]
8	S, N-doped activated $CoFe_2O_4$@CNTs	1,053.60	1	KOH	[73]
9	(NG)/$CuCr_2O_4$	530.6	0.5	H_2SO_4	[74]
10	S doped $MnFe_2O_4$	1,201	2	KOH	This work

the (electrochemical activities) of two samples.

Galvanostatic charge/discharge (GCD) curves of MFO as well as MFO-S are used to measure the capacitive properties of prepared substances, as mentioned in Fig. 5(a)-(b). Both GCD samples curves exhibit evident charging and discharging platforms, proving that they are typical electrode materials for batteries. The specific capacitances of MFO are estimated to be 784.00, 522.6 and 444.27 F g^{-1}, smaller than those of MFO-S, which are estimated to be 1,201.60, 1,014.68 and 914.55 F g^{-1} @ 2, 4 and 5 A g^{-1}, accordingly as displayed in Fig. 5(c). Consequently, C_{sp} of fabricated materials is decreased along with increase of the current density; it could be expected on account of insufficient penetration of electrolyte ions at surface of electrode substance. The relationship between energy as well as power density was measured with Eqs. (3) and (4), and their behavior was explored with the Roenge plot. Their result shows that the power density of the both samples was reduced with rise of E_d as mentioned in Fig. 5(d). Specific capacity of MFO and MFO-S was found to be 450 and 300 C g^{-1}, measured with Eq. (5). The MFO-S GCD stability cycles show rate capability of 97.01% over 2,500 and 95.82% after 5,000 cycles suggests the stable behavior of the electrodes, as depicted in the Fig. 5(e).

ECSA techniques were used to identify the surface area of synthesized materials from 0.9 to 1.10 V (Ag/AgCl) potential window at various scanning speeds of 10 to 40 mV s^{-1}, as mentioned in Fig. 6(a)-(b). Cdl analysis of fabricated substance was calculated by dividing the anodic and cathodic potential. The obtained Cdl value for MFO and MFO-S was 8.71 and 16.21 mF, respectively, as expressed in Fig. 6(c)-(d). Further, Cdl value then was used for computing ECSA of MFO and MFO-S with 217.45 and 405.25 cm^{-2} with the given Eq. (6), respectively.

Fig. 7(a) displays the outcomes of experiments using electrochemical impedance spectroscopy (EIS) on MFO and MFO-S. Curve fits of semicircles in high frequency regions are used to derive the charge transfer resistances (R_{ct}) as well as equivalent series resistances (R_s) of two sample The results show that contact ohmic resistance of electrolyte-electrode interface can be marginally increased due to partial sulfur doping (R_s of MFO and MFO-S are 0.95 Ω and 0.5 Ω), accordingly. Meanwhile, conductivity as well as electrolyte accessibility of active substances, is represented by the R_{ct} values of 1.1 Ω and 0.9 Ω for MFO and MFO-S, respectively. In addition, MFO-S has a steeper performance vs MFO in the low frequency domain, revealing superior capacitive behavior and reduced ion diffusion resistance. Long term stability related to MFO-S electrode was calculated with chronoamperometry @ 0.75 V (Ag/AgCl), as expressed in Fig. 7(b). Results indicate that MFO-S showed small change in the current density of the electrode material in first few hours and then was gradually stable up to 50 h as compared to the IrO_2 as benchmark. The cyclic stability of the electrode material showed also very stable behavior over 5,000 cycles with minor shifting in the current density, and their results are well consistent with

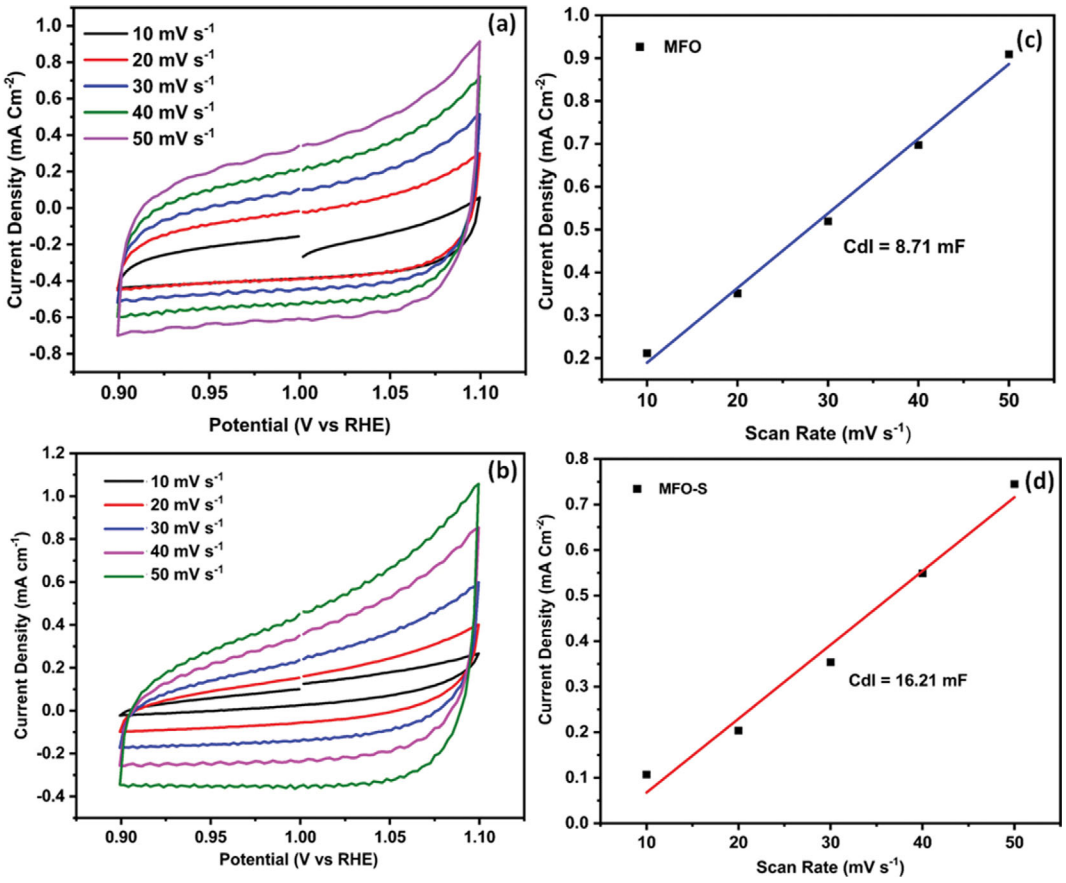

Fig. 6. (a)-(b) CV (c)-(d) Cdl profile of MFO and MFO-S.

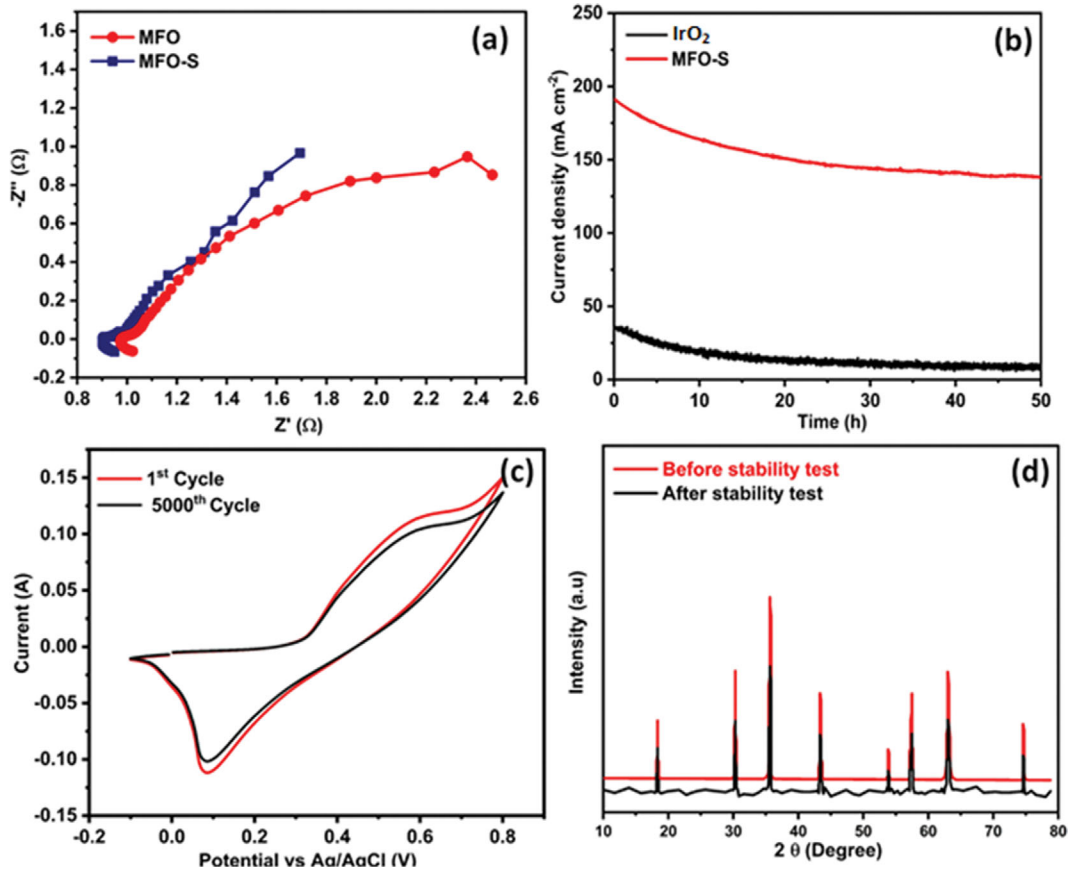

Fig. 7. (a) Nyquist plot, (b) Chronoamperometry of MFO and MFO-S, (c) CV stability cycles, and (d) XRD stabile of MFO-S.

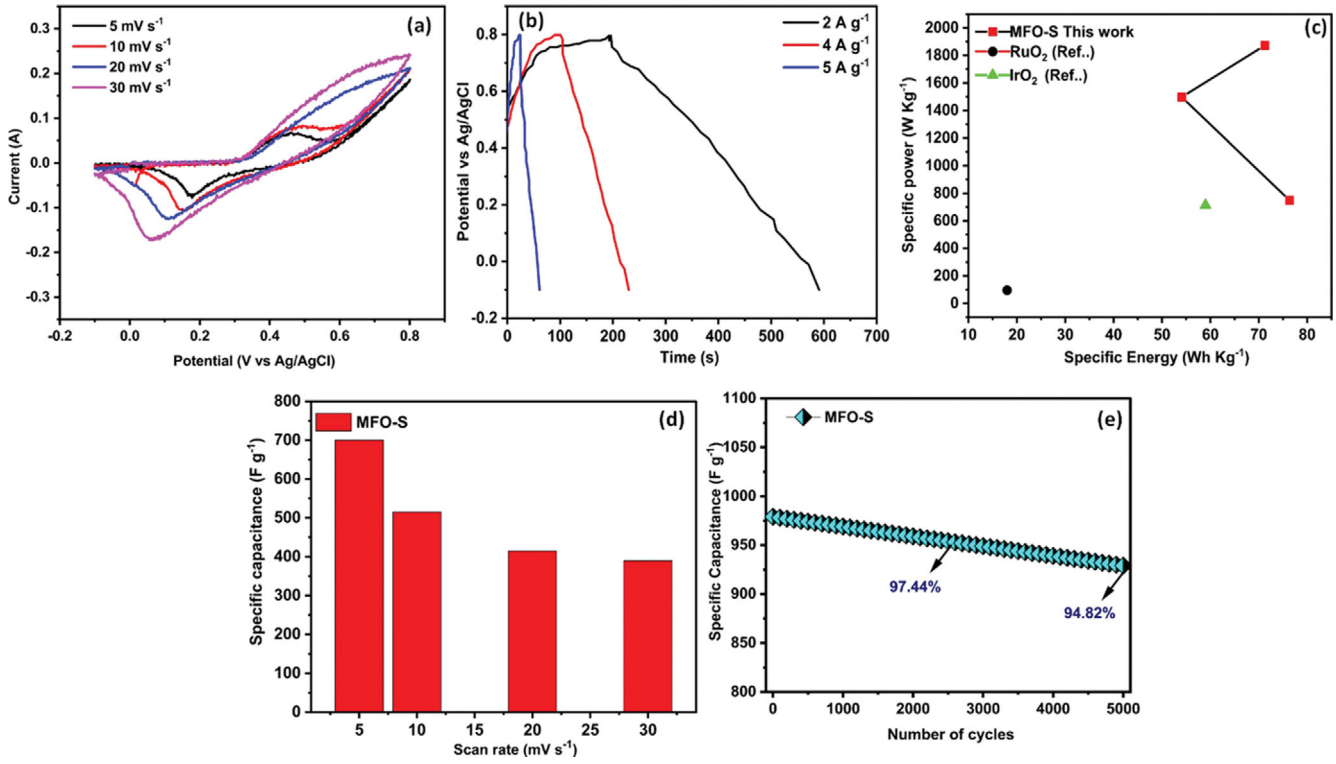

Fig. 8. (a) CV stability cycles, (b) GCD plot profile, (c) Roenge plot, (d) C_{sp} from GCD and (e) GCD stability cycles of MFO-S.

the result of CV stability cycles and chronoamperometry, as shown in Fig. 7(c). Structural stability is a crucial parameter indicating the efficiency of the electrode material. Their results indicate the MFO-S shows stable behavior with little fluctuation in the base line and reduction in intensity, as expressed in Fig. 7(d).

2. Two Electrode Analysis

A two-electrode system was constructed using the acquired MFO-S as anode electrode substance and active carbon as cathode electrode substance that concerns further examining electrochemical performance of the created MFO-S sample via CV curves at multiple scan rate, as mentioned in Fig. 8(a). The findings demonstrate that the voltage windows for MFO-S/AC may vary, ranging in −0.1 to 0.8 V, indicating that the operating voltage window of the material is widely applicable to practical applications. MFO-S/AC exhibited the specific capacitances of 700.27, 514.82, 414.74 and 389.61 F g^{-1} at sweeping speed ranging from 5 to 30 mV s^{-1}. C_{sp} of MFO-S calculated from GCD analysis are 979.97, 694.25 and 914.55 F g^{-1} @ 2, 4, and 5 A g^{-1}, as depicted in Fig. 8(b). As illustrated in Fig. 8(c), P_d along with E_d of samples was estimated employing GCD curves. The Roenge plot shows the relationship between P_d of 749 W kg^{-1} and maximum E_d of MFO-S/AC is 76.35 Wh kg^{-1}, as mentioned in Fig. 8(d). The stability cycle of MFO-S/AC @ 1 A g^{-1} over 5,000 cycles is depicted in Fig. 8(e). It can be perceived from the result that MFO-S/AC steadily decreases to its capacity retention of 97.44% over the course of the first 2,500 cycles, while rate capability over the course of the next 5,000 cycles is up to 94.8%. It is evident that the sample's capacity retention exhibits the same trend as MFO-S/AC, growing at first before stabilizing. All of these good results show that MFO-S/AC has great electrochemical performance and can be used in many different ways.

CONCLUSION

The hydrothermal synthesis method was employed to produce MFO with partial sulfur doping. Morphology of MFO sample changed little after partial sulfur doping. C_{sp} of MFO-S was calculated around 1,201.62 F g^{-1} in three-electrode system at @ 2 A g^{-1}; that was higher in comparison to specific capacitance of MFO, which was 784.0 F g^{-1}. Additionally, in a two-electrode system, C_{sp} of 979.97 F g^{-1}, a maximum E_d of 76.35 Wh kg^{-1} was achieved at P_d of 749 W kg^{-1} @ 2 A g^{-1}. Two and three electrode GCD stability curve shows the 95.82% and 94.82% rate capability after 5,000 cycles, respectively. Our results suggest that partial sulfur doping of $MnFe_2O_4$ might enhance its electrochemical performance. In conclusion, this study offers a workable solution to the weak electrochemical activity of oxide-based spinel and significantly expands the application of oxides for supercapacitors.

ACKNOWLEDGEMENTS

Princess Nourah bint Abdulrahman University, located in Riyadh, Saudi Arabia, is supporting researchers under Project Number (PNURSP2023R55). The authors extend their appreciation to the Research Center for Advanced Materials Science (RCAMS), King Khalid University, Saudi Arabia, for funding this work under grant number KKU/RCAMS/023/23.

DECLARATION

Compliance with Ethical Standards

Yes, this paper complies with the journal's ethical guidelines.

CONFLICT OF INTEREST

The authors declare that they have no conflict of interest.

Research Data Policy and Data Availability Statements

The corresponding author will provide the datasets created during and/or analyzed during the current investigation upon reasonable request.

Author's Contributions

Everyone has contributed equally.

REFERENCES

1. S. Aman, M. B. Tahir, Z. Ahmad, S. Znaidia, N. Ahmad, R. Y. Khosa, M. S. Waheed, S. Manzoor, M. Abdullah and T. A. Taha, *Chin. J. Phys.*, **79**, 531 (2022).
2. S. Manzoor, A. G. Abid, S. Aman, M. Abdullah, A. R. Rashid, H. M. Ali, T. E. Ali, M. A. Assiri, M. N. Ashiq and T. A. Taha, *Ceram. Int.*, **48**, 36975 (2022).
3. S. Gouadria, M. Abudllah, Z. Ahmad, P. John, M. U. Nisa, S. Manzoor, S. Aman, M. N. Ashiq and M. I. Ghori , *Ceram. Int.*, **49**, 4281 (2022).
4. X. Li, Y. Li, X. Zhao, F. Kang and L. Dong, *Energy Storage Mater.*, **53**, 505 (2022).
5. T. Kosukoglu, M. Carpan, S. Riza Tokgoz and A. Peksoz, *Mater. Sci. Eng. B.*, **286**, 116032 (2022).
6. B. T. Al-Abawi, N. Parveen and S. A. Ansari, *Sci. Rep.*, **12**, 1 (2022).
7. W. K. Chee, H. N. Lim, I. Harrison, K. F. Chong, Z. Zainal, C. H. Ng and N. M. Huang, *Electrochim. Acta*, **157**, 88 (2015).
8. J. Liang, Y. Feng, L. Liu, S. Li, C. Jiang and W. Wu, *J. Mater. Chem. A*, **7**, 15960 (2019).
9. G. Qiu, Q. Qiu, L. Qing, J. Zhou, X. Xu and S. Zhao, *J. Phys. Chem. C.*, **19**, 8218 (2022).
10. Y. Chen, H. Yang, Z. Han, Z. Bo, J. Yan, K. Cen and K. K. Ostrikov, *Energy Fuels*, **36**, 2390 (2022).
11. S. A. Beknalkar, A. M. Teli, T. S. Bhat, K. K. Pawar, S. S. Patil, N. S. Harale, J. C. Shin and P. S. Patil, *J. Mater. Sci. Technol.*, **130**, 227 (2022).
12. T. Schoetz, L. W. Gordon, S. Ivanov, A. Bund, D. Mandler and R. J. Messinger, *Electrochim. Acta*, **412**, 140072 (2022).
13. M. M. Baig, I. H. Gul, S. M. Baig and F. Shahzad, *J. Electroanal. Chem.*, **904**, 115920 (2022).
14. M. Y. Zhang, J. Y. Miao, X. H. Yan, Y. H. Zhu, Y. L. Li, W. J. Zhang, W. Zhu, J. M. Pan, M. S. Javed and S. Hussain, *J. Mater. Chem.*, **10**, 640 (2022).
15. R. Yan, M. Antonietti and M. Oschatz, *Adv. Energy Mater.*, **8**, 1800026 (2018).
16. M. Kim and J. Kim, *Phys. Chem. Chem. Phys.*, **16**, 11323 (2014).
17. B. E. Conway and W. G. Pell, *J. Solid State Electrochem.*, **7**, 637 (2003).
18. J. Yan, Z. Fan, W. Sun, G. Ning, T. Wei, Q. Zhang, R. Zhang, L. Zhi

and F. Wei, *Adv. Funct. Mater.*, **22**, 2632 (2012).
19. H. Ren, L. Zhang, J. Zhang, T. Miao, R. Yuan, W. Chen, Z. Wang, J. Yang and B. Zhao, *Carbon N Y.*, **198**, 46 (2022).
20. M. Abdullah, P. John, Z. Ahmad, M. N. Ashiq, S. Manzoor, M. I. Ghori, M. U. Nisa, A. G. Abid, K. Y. Butt and S. Ahmed, *Appl. Nanosci.*, **11**, 2361 (2021).
21. M. U. Nisa, S. Manzoor, A. G. Abid, N. Tamam, M. Abdullah, M. Najam-Ul-Haq, M. S. Al-Buriahi, Z. A. Alrowaili, Z. M. M. Mahmoud and M. N. Ashiq, *Fuel*, **321**, 124086 (2022).
22. X. Xu, W. Liu, Y. Kim and J. Cho, *Nano Today*, **9**, 604 (2014).
23. M. Akhilash, P. S. Salini, B. John and T. D. Mercy, *J. Alloys Compd.*, **869**, 159239 (2021).
24. P. Geng, S. Zheng, H. Tang, R. Zhu, L. Zhang, S. Cao, H. Xue and H. Pang, *Adv. Energy Mater.*, **8**, 1703259 (2018).
25. B. wen Deng, Y. Yang, B. Yin and M. bo Yang, *J. Colloid Interface Sci.*, **594**, 770 (2021).
26. D. Zheng, C. Sun, W. Pan, G. Guo, Y. Zheng, C. Liu and J. Zhu, *Energy Fuels*, **35**, 16915 (2021).
27. X. Li, X. Li, G. Wang, X. Wang and J. Ji, *J. Mater. Chem. A*, **1**, 10103 (2013).
28. D. P. Mali, R. T. Patil, A. S. Patil and V. J. Fulari, Chem. *Phys. Lett.*, **770**, 138431 (2021).
29. D. Zhou, H. Lin, F. Zhang, H. Niu, L. Cui, Q. Wang and F. Qu, *Electrochim. Acta*, **161**, 427 (2015).
30. K. H. Ye, Z. Q. Liu, C. W. Xu, N. Li, Y. B. Chen and Y. Z. Su, *Inorg. Chem. Commun.*, **30**, 1 (2013).
31. Y. C. Chen, Y. K. Hsu, Y. G. Lin, Y. K. Lin, Y. Y. Horng, L. C. Chen and K. H. Chen, *Electrochim. Acta*, **56**, 7124 (2011).
32. C. Justin Raj, R. Manikandan, P. Sivakumar, D. O. Opar, A. Dennyson Savariraj, W. J. Cho, H. Jung and B. C. Kim, *J. Alloys Compd.*, **892**, 162199 (2022).
33. X. Gao, W. Wang, J. Bi, Y. Chen, X. Hao, X. Sun and J. Zhang, *Electrochim. Acta*, **296**, 181 (2019).
34. S. S. Raut and B. R. Sankapal, *Electrochim. Acta*, **198**, 203 (2016).
35. S. Maitra, R. Mitra and T. K. Nath, *Curr. Appl. Phys.*, **27**, 73 (2021).
36. M. Fei, R. Zhang, L. Li, J. Li, Z. Ma, K. Zhang, Z. Li, Z. Yu, Q. Xiao and D. Yan, *Electrochim. Acta*, **368**, 137586 (2021).
37. D. P. Sherstyuk, A. Y. Starikov, V. E. Zhivulin, D. A. Zherebtsov, S. A. Gudkova, N. S. Perov, Y. A. Alekhina, K. A. Astapovich, D. A. Vinnik and A. V. Trukhanov, *Ceram. Int.*, **47**, 12163 (2021).
38. M. Hassan, Y. Slimani, M. A. Gondal, M. J. S. Mohamed, S. Güner, M. A. Almessiere, A. M. Surrati, A. Baykal, S. Trukhanov and A. Trukhanov, *Ceram. Int.*, **48**, 24866 (2022).